Supporting Information for

Unveiling Planar Defects in Hexagonal Group IV Materials

Elham M. T. Fadaly[1‡], Anna Marzegalli[2,3‡], Yizhen Ren[1], Lin Sun[4], Alain Dijkstra[1], Diego de Matteis[5], Emilio Scalise[3], Andrey Sarikov[3,6], Marta De Luca[5], Riccardo Rurali[7], Ilaria Zardo[5], Jos E. M. Haverkort[1], Silvana Botti[4], Leo Miglio[3], Erik P. A. M. Bakkers[1], Marcel A.Verheijen[1,8*]

[1] Department of Applied Physics, Eindhoven University of Technology, 5600 MB Eindhoven, the Netherlands
[2] Dipartimento di Fisica, Politecnico di Milano, via Anzani 42, 22100 Como, Italy
[3] L-NESS and Dipartimento di Scienza dei Materiali, Università di Milano-Bicocca, Via R. Cozzi 55, 20125 Milano, Italy
[4] Institut für Festkörpertheorie und -optik, Friedrich-Schiller-Universität Jena, Max-Wien-Platz 1, 07743 Jena, Germany
[5] Departement Physik, Universität Basel, Klingelbergstr. 82, 4056 Basel, Switzerland
[6] V. Lashkarev Institute of Semiconductor Physics, National Academy of Sciences of Ukraine, 45 Nauki avenue, 03028 Kyiv, Ukraine
[7] Institut de Ciència de Materials de Barcelona, ICMAB-CSIC, Campus UAB, 08193 Bellaterra, Spain
[8] Eurofins Materials Science Netherlands BV, High Tech Campus 11, 5656 AE Eindhoven, the Netherlands
[‡] These authors contributed equally to this work
*Correspondence to: m.a.verheijen@tue.nl

This file includes:

Methods

Materials Synthesis
TEM Characterization
Molecular Dynamics Simulations
Stacking Fault Energy Calculations
Electronic Band Structure Calculations
Experimental Raman Spectroscopy Measurements
Theoretical Raman Calculations

Supporting Information

Section S1: I_3 BSF Visualization under Different Imaging Modes
Section S2: Comparison of I_3 BSF with the Literature
Section S3: Defects Quantification and Defects Volume Fraction Calculations

Supporting Figures

Supporting Figure 1: I_3 BSFs and Terminating Dislocations in Hex-Si
Supporting Figure 2: Evidence of the I_3 BSFs Absence in the WZ-GaAs Core Nanowires
Supporting Figure 3: Tracing the Origin of the I_3 BSF
Supporting Figure 4: Imaging the I_3 BSF and its *T*erminations under 60° Viewing Direction
Supporting Figure 5: Spatial and Intensity Analysis of the Atomic Stacking of I_3 Defects Imaged under Two Different Orientations
Supporting Figure 6: Summary of the Different Projected Atomic Configurations of the I_3 BSF and its *T*erminating *D*islocation**s**
Supporting Figure 7: Visualization of the Double Plane Stacking Fault
Supporting Figure 8: Different Types of BSFs in a Slab of Hex-Ge
Supporting Figure 9: Band Structure Calculation of Hex-Si and Hex-Ge Crystals With and Without I_3 BSFs and its Terminating Dislocations
Supporting Figure 10: Representative TEM images of the Characterized Samples by Raman Spectroscopy
Supporting Figure 11: Defects Quantification and Volume Fraction Calculation
Supporting Figure 12: Theoretically Calculated Raman Spectra of Defect free and I_3 Defected Hex-Ge cells

Methods

Materials Synthesis

The GaAs and GaP nanowires were grown in a low pressure (50 mbar) Aixtron close coupled shower head (CCS) MOVPE reactor via catalyst assisted growth following the Vapor-Liquid-Solid (VLS) mechanism utilizing gold (Au) catalyst seeds. The Au catalyst seeds were deposited in nano disks arrays arrangement on a GaAs (111)B substrate for the GaAs/Ge nanowires and GaP (111)B/SiN substrate for the GaP/Si via the electron beam lithography technique. The growth was performed at a reactor flow of 8.2 standard litres per minute (slm) utilizing hydrogen (H_2) as the carrier gas. For the GaAs nanowires, the growth template was annealed at thermocouple set temperature of 635°C under an AsH_3 flow set to a molar fraction of $\chi_{AsH_3}=6.1\times10^{-3}$. Then, the WZ-GaAs nanowires growth was performed at a temperature of 615°C with TMGa and AsH_3 as material precursors set to molar fractions of $\chi_{TMGa}=1.9\times10^{-5}$, $\chi_{AsH_3}=4.55\times10^{-5}$, respectively, achieving a total flux V/III ratio of 2.4.

After the growth of the GaAs/GaP core nanowires, they are chemically treated with a diluted potassium cyanide (KCN) aqueous solution to remove the Au particles to avoid gold contamination. Eventually, the GaAs or GaP nanowire cores are used as a hexagonal material template and are overgrown with a Ge or Si shell by introducing the suitable gas precursors for the shell growth, 1% diluted germane (GeH_4) in the case of a Ge shell and 1% diluted tetrasilane (Si_4H_{10}) in the case of a Si shell. The Ge shells were grown at a thermocouple set temperatures in the range of 500-650 °C at a germane molar fraction of $\chi_{Ge}=8.5\times10^{-7}$ for a certain growth period according to the desired shell volume. The hex-GaP/Si core/shell growth details are reported elsewehre[1].

TEM Characterization

For the TEM studies, two different sample preparation methods were used. In the standard axial analysis, nanowires were mechanically transferred from the growth substrate to a holey carbon TEM grid. Concerning the cross-section TEM studies, nanowires were prepared using Focused Ion Beam (FIB). In both cases, HR-TEM and STEM analyses were conducted using a JEM ARM200F probe-corrected TEM operated

at 200 kV. For the chemical analysis, EDX measurements were carried out using the same microscope equipped with a 100 mm^2 EDX silicon drift detector.

TEM lamellae were prepared in a FEI Nova Nanolab 600i Dual beam system. For this, the nanowires are initially transferred with the aid of a micromanipulator from the growth substrate to a piece of Si and then arranged to lie parallel to each other. These nanowires are then covered with electron- and ion-beam induced metal deposition to protect them during the focused ion beam cutting procedure. The lamella is cut out by milling with 30 kV Ga ions and thinned down with subsequent steps of 30, 16, and 5 kV ion milling in order to minimize the Ga-induced damage in the regions imaged with TEM.

Molecular Dynamics Simulations

Hexagonal prismatic simulation cell sideways faceted by the {1-100} planes, representing hex-Ge nanowire has been used in atomic simulations using molecular dynamics approach. Two partial dislocation pairs have been placed into the same double plane of the cell separated by an I_3 stacking fault naturally formed between them as a result of their insertion. Each dislocation pair is formed by two 30° partial glide dislocations with opposite Burgers vector situated one above another in consecutive lattice planes in the <0001> direction. The directions of dislocation lines correspond to $[\bar{1}2\bar{1}0]$ and $[11\bar{2}0]$ for the first and second pair, respectively.

The simulation cell with inserted defects has been subjected to energy minimization procedure with the Tersoff potential for Ge, applying the Polak-Ribiere conjugate gradient algorithm (stopping tolerance for energy and force were equal to 10^{-6} and 10^{-8} eV/Å, respectively)[2]. Because of the absence of empirical potentials fitted for hex-Ge phase, we have used the Tersoff potential for cubic diamond Ge. However, as this potential takes into account the interactions of only nearest-neighbor atoms, the configuration of which is the same in both cubic and hexagonal phases, its applicability also for hex-Ge phase is expected. To perform the energy minimization, Large-scale Atomic/Molecular Massively Parallel Simulator (LAMMPS) code for molecular dynamics simulations has been used[3].

Stacking Fault Energy Calculations

The calculations of the formation energy of different SFs were performed with DFT and planewave basis sets as implemented in the Quantum Expresso code[4]. The exchange-correlation was treated in the generalized gradient approximation (GGA) as parameterized by Perdew *et al.*[5]. A plane-wave cutoff of 80Ry and a 16×16×1 **k**-point grid was used. The supercells used for the atomistic simulations of the SFs, partially illustrated in the **Supporting Information Fig. 6 were** created from a 1X1X6 periodic replica of the unit cell of hex-Ge (Si) and including different SFs configurations. The calculated formation energies of the single SFs in the two different configurations shown in **Supporting Information Fig. 6a and Fig. 6b** are -3.19 mJ/m^2 and -6.14 mJ/m^2 (-2.71 mJ/m^2 and -4.72 mJ/m^2 for Si) respectively, and thus roughly proportional to the row number of cubic sites formed in between Ge layers that are marked in the figures. Note that the cubic sites denote the cubic local symmetry, in agreement with the h-c *Jagodzinski* notation[6]. Obviously, the symmetry of all the other pristine stacking layers in the 2*H* crystal is hexagonal, even if not explicitly indicated in the **Supporting Information Fig. 6.** The double SF shown in **Supporting Information Fig. 6c**, forming the I_3 BSF*,* 21is also characterized by two rows of cubic sites and has a formation energy of -6.32 mJ/m^2 (-5.38 mJ/m^2 for Si), thus comparable to that of the SF in (b) and about two times the value of the formation energy of the single SF in **Supporting Information Fig. 6a**. Then, the formation of two single SFs as illustrated in (d) is thermodynamically equivalent to the I_3 BSF and slightly favored than the SF in (b), if no dislocations are considered. Indeed, during a planar growth (in the vertical direction of the figures and corresponding to the <0001> direction) on top of a stacking fault plane the crystal can freely continue to incorporate atoms in any stacking sequence and having two separate single SFs as in (d) or the double one is not very different from the thermodynamic point of view. On the contrary, in case of the nanowire radial growth, one should see a growth front in the radial directions (perpendicular to the <0001> direction), thus the growing crystal containing the SF planes has to connect to the material deposited previously, which should form a perfect hexagonal crystal. Then, to have a configuration with two separate SFs as in (d), a column of dislocations in between the two stacking faults must be formed. Instead, the double layer SF with the terminating dislocation pair as in (c) is the natural configuration

minimizing the number of dislocations (and their energy, being null in total Burgers vector) and it is thus favored in the radial growth. Instead a sessile dislocation with Burgers vector out of the glide plane, thus having high formation energy, has to be formed to connect the SF in (b) to the perfect crystal, consequently this single SF is also unfavored as compared to the I_3 BSF[7].

Electronic Band Structure Calculations

Band structure calculations were performed using the Vienna *Ab initio* Simulation Package (VASP), which implements DFT within the projector-augmented wave method[8,9]. We set the plane-wave cutoff to 500 eV and included Ge 3d electrons as valence electrons. The supercell model for the defect contains 384 Ge atoms and it was relaxed using the minima hopping method for crystal structure prediction calculating energies and forces with the DFT tight-binding code DFTB+[10–12]. For this task we employed Slater-Koster parameters specifically developed to obtain accurate energies and forces[13]. The lowest energy geometry was then relaxed again using VASP with the Perdew-Burke-Ernzerhof (PBE) exchange-correlation functional[5].

A Γ-centered 3×2×2 **k**-point grid was used, and the calculation was converged until the energy difference of two electronic SC steps was less than 0.1 meV. The functional that we use for band structure calculations is the meta-GGA functional MBJLDA of Tran and Blaha, which gives an excellent band structure for diamond and hex-Ge[14,15]. Spin-orbit coupling increases the band gap of hex-Ge by 0.09 eV, while there is no significant effect on band dispersion. Due to the difficulty to converge MBJLDA calculations for large supercells including spin-orbit, we performed these calculations neglecting spin-orbit coupling, and added then a correction of -0.09 eV to account for the renormalization effect on the band gap. The band diagrams show the local density of states (LDOS) along the $\{10\bar{1}0\}$ crystallographic direction, averaged in the perpendicular plane, as obtained from MBJLDA calculations. We convoluted the LDOS with a Gaussian smearing of 0.1 eV.

Experimental Raman Spectroscopy Measurements

Raman scattering measurements were performed on single GaAs/Ge core/shell nanowires at room temperature. The light source was the 514 nm line of an Ar-Kr ion laser, focused onto the samples through a high numerical aperture (0.95) 100x objective with a working distance of 0.3 mm. The beam power, polarization of the incident, and backscattered light were controlled with neutral density filters and polarization optics. The spectra of all nanowires were recorded with the same acquisition times while always keeping a low incident laser power of 38 μW in order to avoid heating effects or damage to the nanowires. For the spectra presented in this work, the exciting and scattered light were both polarized perpendicular to the nanowire growth axis (namely, polarized in the Y direction in our reference system). The signal was collected by a T64000 Horiba triple spectrometer working in a subtractive mode, equipped with 1800 g mm^{-1} diffraction gratings and with a liquid nitrogen cooled multichannel CCD detector. The spectrometer in this configuration has a spectral resolution of 0.5 – 1 cm^{-1}.

Theoretical Raman Calculations

The ground state geometry of hex-Ge has been obtained from density-functional theory calculations (DFT) performed with the Abinit code[16,17] using the local-density approximation (LDA) and norm-conserving pseudopotentials[18]. We used a 38 Ha plane-wave cutoff and sampled the Brillouin zone with a 16×16×12 **k**-point grid. After the relaxation the forces on the atoms and the components of the stress tensor were lower than 3·10-5 eV/Å and 4.5·10-4 GPa, respectively. We then computed the Raman susceptibility tensors within density-functional perturbation theory (DFPT)[19] from the third derivative of the total energy, twice with respect to the application of an electric field and once with respect to the phonon displacement coordinates, making use of the 2n+1 theorem as implemented in the Abinit code[20]. Given the sensitivity of the energy derivative to the quality of the converged wavefunctions, we imposed a strict convergence criterion of the wavefunction residual norm of 10-22. The k-grid that we used is shifted along k_x, k_y, and k_z, so that the Monkhorst-Pack algorithm does not select any k-point where the bandgap of Ge vanishes due self-interaction and the calculation of the Raman

susceptibility can be performed. It was previously shown in hex-Si that this choice does not affect the results and that the differences with the Raman spectra obtained using a k-grid that features a shift only along k_z and is G-centered in the (k_x, k_y) plane — and that is thus consistent with the hexagonal symmetry of the lattice — are negligible[21].

Supporting Information

S1: I_3 BSF Visualization under Different Imaging Modes

There is one apparent contradiction between the results of imaging the I_3 BSFs in the two different imaging modes BFTEM and HAADF-STEM that needs to be addressed here. In the reconstruction of the 2-D shape of the planar defects in **Fig. 2c** in the main text, it is evident that the defects do not extend over the entire thickness of the nanowire. However, in the high-resolution STEM images, we do not see a superposition of the defect geometry with that of a defect-free lattice. The reason for this is the depth-of-focus of an aberration-corrected STEM operated at 200 kV, being in the order of 11 nm[22]. Thus, by focusing on the nanowire's entrance surface, this first 11 nm will dominate the information in the image.

S2: Comparison of I_3 BSF with the literature

In previous work, a defect was reported in hex-Si nanowires that was interpreted to be the manifestation of a ‘crack,’ a local, small gap between individual atomic planes[23]. To investigate whether the defect in our material systems is of a similar nature as the crack defect, complementary high-resolution TEM and HAADF-STEM imaging of the same defect in addition to spatial and intensity analysis of the atomic stacking was conducted as discussed in **Supporting Information Fig. 3 and 4**. This study concludes that the I_3 BSF results in the same contrast as the previously reported crack. Accordingly, we deduce that HAADF-STEM imaging is required to uniquely identify the nature of planar defects in hexagonal group IV materials. Besides, very recently, in 2018, the termination of the same I_3 BSF has been observed in the defective top part of zincblende GaAsP/GaAsP core/shell nanowires in the high-resolution STEM mode, together with 21 kinds of other defects in the same region of the crystal, formed in the final, non-equilibrium

stage of the growth[24]. The authors described the zero Burgers vector nature of this defect and hypothesized it could be formed by the loss of monolayer-by-monolayer growth in the vertical direction. This explanation does not apply to our core-shell nanowires, as no nucleation of new close-packed layers is required for the epitaxial growth from the sidewalls. In our hex-Si, -Ge and -SiGe shells, the I_3 BSF is the planar defect type present. This is also the first time that the I_3 BSF stacking fault and its terminating dislocations are observed in group four material.

S3: Defects Quantification and Defects volume fraction calculations

The I_3 BSFs are quantified from the TEM images of the corresponding Raman characterized samples. The TEM images are acquired in the scanning TEM mode (STEM). The I_3 defects density is quantified such that all partial defect lines apparent in the STEM images are counted on both sides of the shell in the imaged GaAs/Ge core/shell structure segment. All the I_3 defects quantification is based on STEM images of segments of the nanowires, as elucidated in **Supporting Fig. 9**. Therefore, each defect volume fraction reported is based on the defects volume in this segment of the nanowire with respect to the corresponding segment volume of the hex-Ge shell structure, see **Eq. 1**.

$$I_3 \text{ Volume fraction } \% = \frac{V_{I3}}{V_{\text{shell}}} * 100\% \quad (1)$$

The core/shell structure is approximated in calculations as two concentric cylinders, for simplification, see **Supporting Fig. 10a**. Hence, the volume of the core and the shell is calculated as the volume of a circular cylinder as explained in **Eq. 2-4**:

$$V_{\text{core}} = \pi \, r_{\text{core}}^2 * L_{segment} \quad (2)$$

$$V_{\text{core/shell}} = \pi \, r_{\text{core/shell}}^2 * L_{segment} \quad (3)$$

$$V_{\text{shell}} = V_{\text{core/shell}} - V_{\text{core}} \quad (4)$$

As explained in the main text, the I_3 BSF is a planar stacking fault with two terminating partial dislocation pairs separated by 60°, consisting of two Ge layers. Hence,

we can approximate the volume of I_3 BSF (V_{I_3}) as the volume of a triangular prism with an equilateral triangular base, see **Supporting Fig 9b.** The side length of the equilateral triangle is equivalent to the extension length of the I_3 BSF in the hex-Ge shell (l_{I3}), viewed in the <$11\bar{2}0$> zone axis. The height of the prism (*h*), equivalent to the thickness of the I_3 BSF plus two non-defected layer, is approximately equivalent to the out of plane lattice parameter *c* of the 4*H*-polytype of hex-Ge, which is approximately double the c-parameter of 2*H* hex-Ge, reported in Ref.[25]. Hence, the volume of I_3 BSF can be approximated as explained in **Eq. 5**:

$$V_{I_3} = \frac{\sqrt{3}}{4} \cdot h \cdot l_{I_3}^2 \text{ ; where } h = 2.c \tag{5}$$

For the simplification of the defects' quantification process, we assume all defects to start at the interface and extend to their maximum length which is equivalent to the shell thickness. This assumption is based on the fact that the I_3 defects, visualized in the STEM images of the samples characterized by Raman, mostly start at the interface and a few percentages starts later at the shell. Hence, we take the maximum length extension as an upper bound for the defect length. Hence, the calculation of the defects volume fraction in the shell might be overestimated. On the other hand, due to the limited depth of focus of the STEM imaging mode, not all defects are in focus especially in quite thick core/shell structures. Hence, not all defects are in focus, so we might have missed to quantify a portion of the defect which is an underestimation of the number of defects. Tiny defects, initiated at the end of the shell growth process most probably won't be visible, because of the limited diffraction contrast. This effect may be larger for thicker wires. However, the volume contribution of these smaller defects is quite small, because of their limited lateral size. Hence, we can rewrite **Eq. 5** as explained in **Eq. 6**:

$$V_{I_3} = \frac{\sqrt{3}}{2} \cdot h \cdot r_{shell}^2 . c \tag{6}$$

References

1. Ren, Y., Leubner, P., Verheijen, M. A., Haverkort, J. E. M. & Bakkers, E. P. A. M. Hexagonal silicon grown from higher order silanes. *Nanotechnology* **30**, 295602 (2019).
2. Tersoff, J. New empirical approach for the structure and energy of covalent systems. *Phys. Rev. B* **37**, 6991–7000 (1988).
3. Plimpton, S. Fast parallel algorithms for short-range molecular dynamics. *J. Comput. Phys.* **117**, 1–19 (1995).
4. Giannozzi, P. *et al.* QUANTUM ESPRESSO: A modular and open-source software project for quantum simulations of materials. *J. Phys. Condens. Matter* **21**, 395502 (2009).
5. Perdew, J. P., Burke, K. & Ernzerhof, M. Generalized gradient approximation made simple. *Phys. Rev. Lett.* **77**, 3865–3868 (1996).
6. Jagodzinski, H. Eindimensionale Fehlordnung in Kristallen und ihr Einfluss auf die Röntgeninterferenzen. I. Berechnung des Fehlordnungsgrades aus den Röntgenintensitäten. *Acta Crystallogr.* **2**, 201–207 (1949).
7. Zakharov, D. N. *et al.* Structural TEM study of nonpolar a-plane gallium nitride grown on $(11\bar{2}0)$4H-SiC by organometallic vapor phase epitaxy. *Phys. Rev. B - Condens. Matter Mater. Phys.* **71**, 235334 (2005).
8. Kresse, G. & Furthmüller, J. Efficient iterative schemes for ab initio total-energy calculations using a plane-wave basis set. *Phys. Rev. B - Condens. Matter Mater. Phys.* **54**, 11169–11186 (1996).
9. Kresse, G. & Joubert, D. From ultrasoft pseudopotentials to the projector augmented-wave method. *Phys. Rev. B* **59**, 1758–1775 (1999).
10. Goedecker, S. Minima hopping: An efficient search method for the global minimum of the potential energy surface of complex molecular systems. *J. Chem. Phys.* **120**, 9911–9917 (2004).
11. Aradi, B., Hourahine, B. & Frauenheim, T. DFTB+, a sparse matrix-based implementation of the DFTB method. in *Journal of Physical Chemistry A* **111**, 5678–5684 (2007).
12. Amsler, M. & Goedecker, S. Crystal structure prediction using the minima hopping method. *J. Chem. Phys.* **133**, 224104 (2010).
13. Huran, A. W., Steigemann, C., Frauenheim, T., Aradi, B. & Marques, M. A. L. Efficient Automatized Density-Functional Tight-Binding Parametrizations: Application to Group IV Elements. *J. Chem. Theory Comput.* **14**, 2947–2954 (2018).
14. Tran, F. & Blaha, P. Accurate band gaps of semiconductors and insulators with a semilocal exchange-correlation potential. *Phys. Rev. Lett.* **102**, (2009).

15. Rödl, C. *et al.* Accurate electronic and optical properties of hexagonal germanium for optoelectronic applications. *Phys. Rev. Mater.* **3**, 034602 (2019).

16. Gonze, X. *et al.* ABINIT: First-principles approach to material and nanosystem properties. *Comput. Phys. Commun.* **180**, 2582–2615 (2009).

17. Veithen, M., Gonze, X. & Ghosez, P. Nonlinear optical susceptibilities, Raman efficiencies, and electro-optic tensors from first-principles density functional perturbation theory. *Phys. Rev. B - Condens. Matter Mater. Phys.* **71**, 125107 (2005).

18. Troullier, N. & Martins, J. L. Efficient pseudopotentials for plane-wave calculations. *Phys. Rev. B* **43**, 1993–2006 (1991).

19. Baroni, S., De Gironcoli, S., Dal Corso, A. & Giannozzi, P. Phonons and related crystal properties from density-functional perturbation theory. *Rev. Mod. Phys.* **73**, 515–562 (2001).

20. Gonze, X. & Vigneron, J. P. Density-functional approach to nonlinear-response coefficients of solids. *Phys. Rev. B* **39**, 13120–13128 (1989).

21. Fasolato, C. *et al.* Crystalline, Phononic, and Electronic Properties of Heterostructured Polytypic Ge Nanowires by Raman Spectroscopy. *Nano Lett.* **18**, 7075–7084 (2018).

22. Xin, H. L. & Muller, D. A. Three-dimensional imaging in aberration-corrected electron microscopes. in *Microscopy and Microanalysis* **16**, 445–455 (2010).

23. Conesa-Boj, S. *et al.* Cracking the Si shell growth in hexagonal GaP-Si core-shell nanowires. *Nano Lett.* **15**, 2974–2979 (2015).

24. Sanchez, A. M. *et al.* Stable Defects in Semiconductor Nanowires. *Nano Lett.* acs.nanolett.8b00620 (2018). doi:10.1021/acs.nanolett.8b00620

25. Fadaly, E. M. T. *et al.* Direct-bandgap emission from hexagonal Ge and SiGe alloys. *Nature* **580**, 205–209 (2020).

Supporting Figures

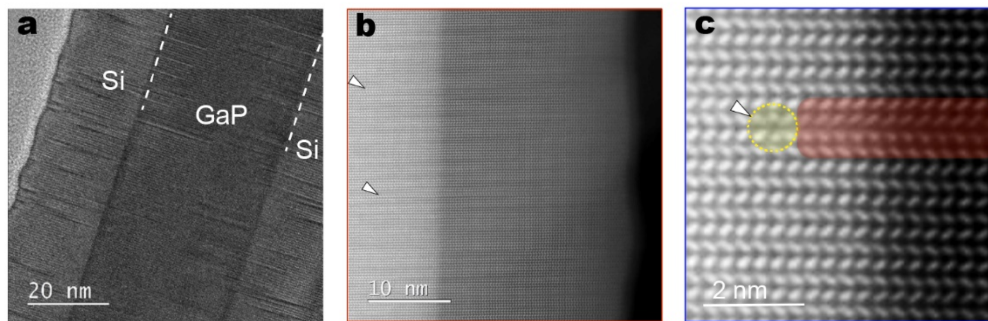

Supporting Figure 1: I_3 BSFs and Terminating Dislocations in Hex-Si: (a) Bright Field TEM image of a representative GaP/Si Core/Shell structure, with white dashed lines indicating the interfaces as a guide for the eye. (**b)** HAADF-STEM image of the GaP/Si structure obtained in the <$11\bar{2}0$> zone axis. (**c)** A magnified image of the framed region in (b) on the left displaying the –ABAB– stacking of the hexagonal structure; The atomic layers colored in white is the faulty stacked bilayer of the I_3 defect. The encircled region displays the I_3 partial dislocation, identical to the case described for hex-Ge.

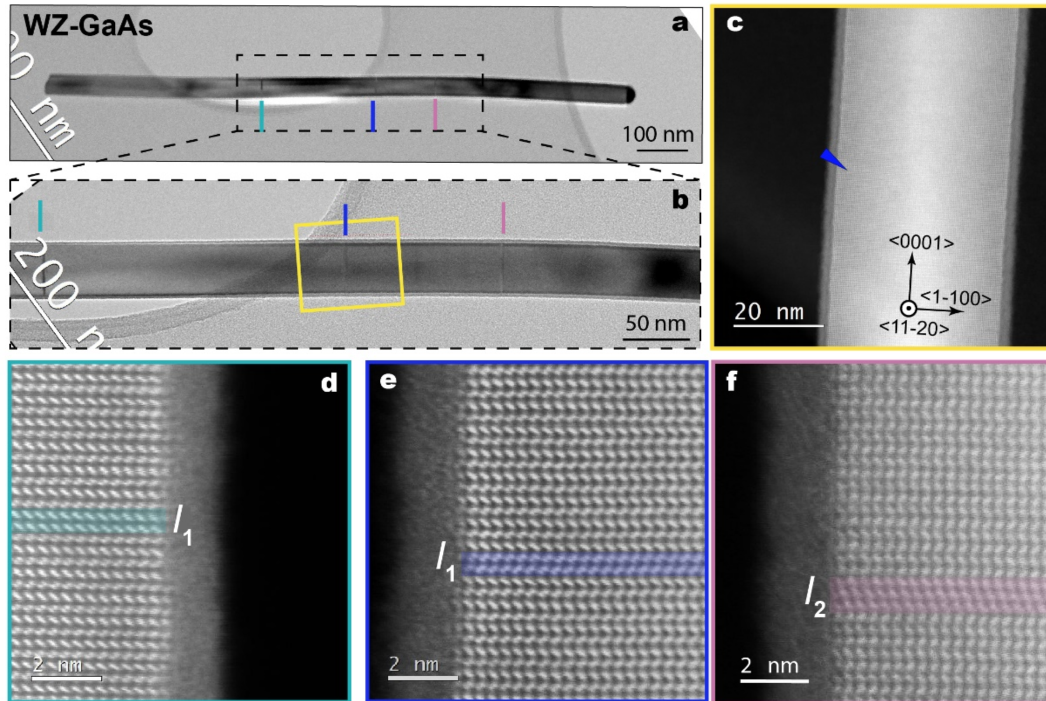

Supporting Figure 2. Evidence of the I_3 BSFs Absence in the WZ-GaAs Core Nanowires: (a) A BF-TEM image of a representative WZ-GaAs core nanowire with three planar SFs along the whole diameter of the nanowire, whose positions are indicated by colored vertical lines. **(b)** A zoomed-in view of the framed region in panel (a) with a black dashed rectangle. **(c)** A HAADF-STEM image of the framed region in panel (b) in yellow, indicating the absence of the partial bright lines, which is usually indicative of I_3 defected nanowires. The blue arrow refers to one of the planar SFs in panels (a, b). The dominant types of these planar defects are presented in panels (d-f). **(d-f)** Magnified HAADF-STEM images of the regions in the WZ crystal of the core nanowire containing the planar SFs of types I_1 and I_2. A different color highlights the atomic stacking of each SF. The stacking of I_1 (AB**<u>ABC</u>**BC) and I_2 stacking (AB**<u>ABCA</u>**CA) is clearly different from the I_3 BSF stacking (AB**<u>ABCBA</u>**BA) presented in the main manuscript.

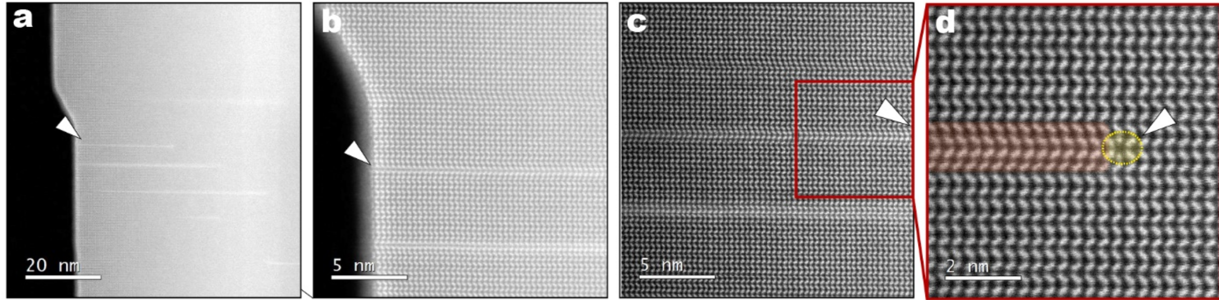

Supporting Figure 3: Tracing the Origin of the *I*$_3$ BSF: (a-d) Aberration-corrected HAADF-STEM images obtained in the <$11\bar{2}0$> zone axis tracing an *I*$_3$ BSF in a hex-Ge crystal appearing as a bright white line and indicated by a white arrow. As we follow this bright line inwards from the edge of the shell, we find out that the defect extends from the interior of the hexagonal shell to the edge of the structure. The highlighted region in (d) in white represents the *I*$_3$ SF and its terminating dislocations. As a result of the presence of partial dislocations indicated by the white arrow, a four-layer stacking resembling the 4*H*-polytope is formed as shown in the highlighted region in white.

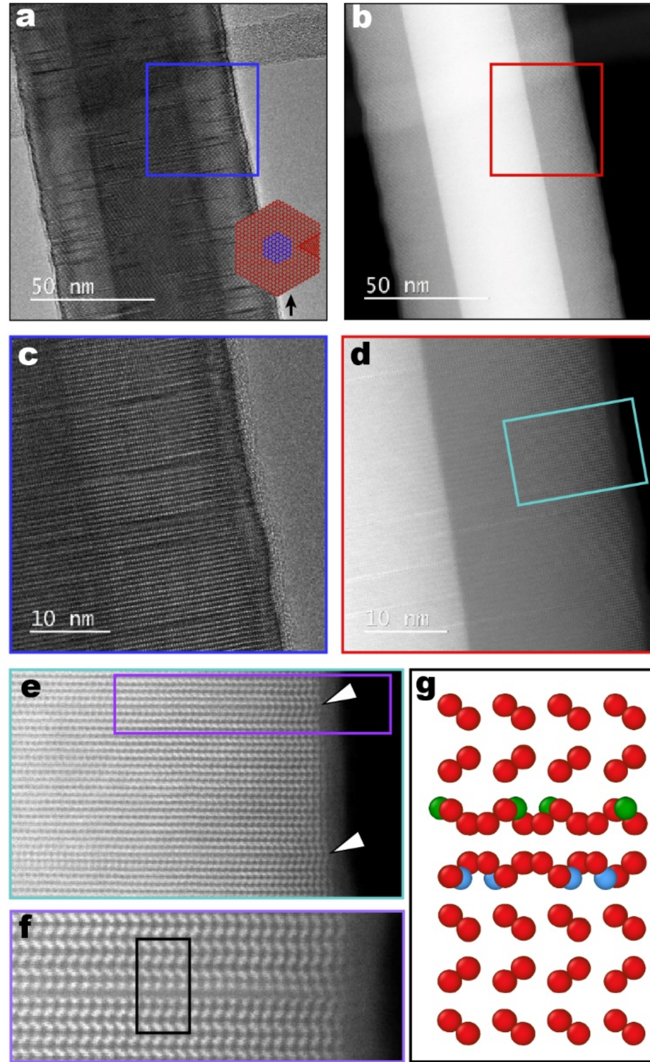

Supporting Figure 4: Imaging the I_3 BSF and its Terminations under 60° Viewing Direction: (a, c) BFTEM images of several I_3 defects in a hex-Si shell, formerly named 'cracks'. Contrasts are identical to those described in Ref. [23]. The inset cartoon in panel (a) represents the imaging direction of these defects in the shell part of the nanowire: imaging is performed along a $<11\bar{2}0>$ zone axis. The partial dislocations are imaged under a 60° viewing angle. (**b, d)** HAADF-STEM corresponding to the same region imaged in a, c images. (**e, f)** Zoomed-in HAADF-STEM images for the framed regions in cyan in (d) showing two defects. (**f)** Atomic resolution image of the partial defect framed in (e). (**g)** Atomic model of the atomic arrangement for the defect in (f) in this viewing direction, based on the defect geometry as discussed in detail in **Fig. 3** of the main text**.** Green and light blue atoms belong to the dislocation cores.

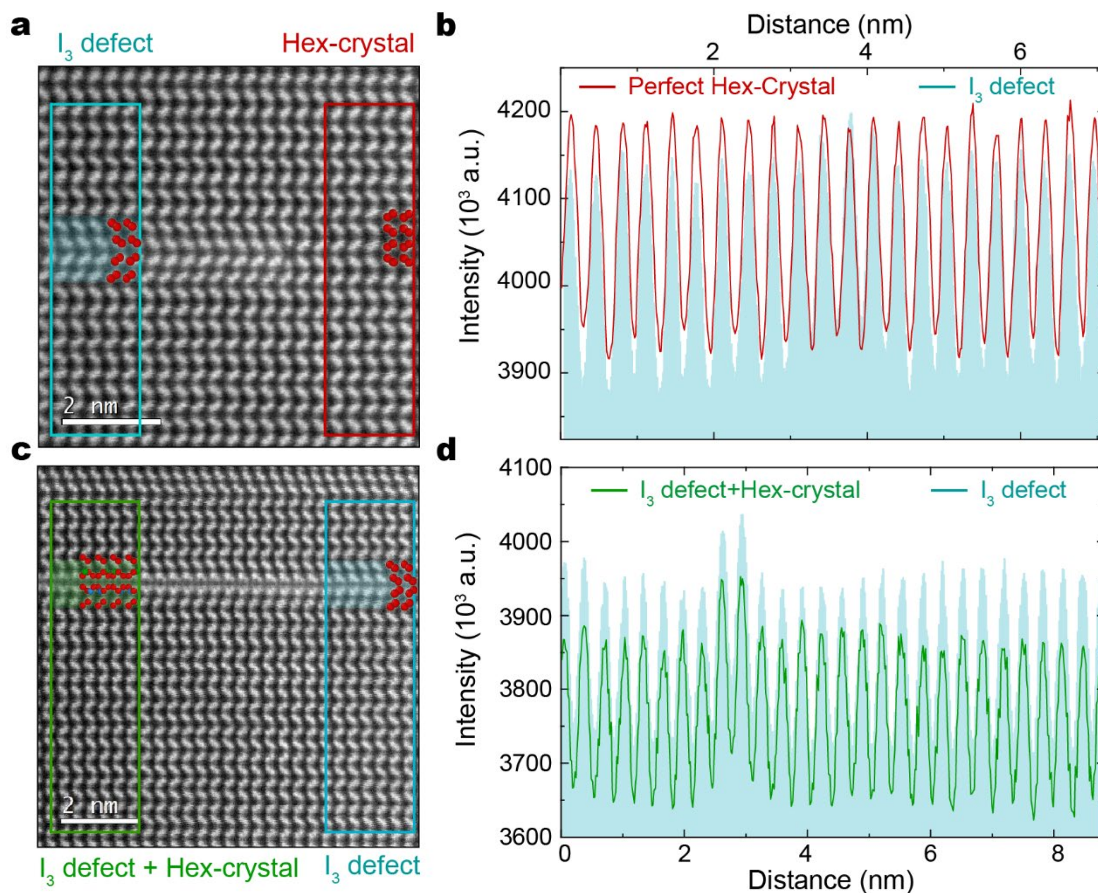

Supporting Figure 5: Spatial and Intensity Analysis of the Atomic Stacking of *I*3 Defects Imaged under Two Different Orientations: (**a, c)** HAADF-STEM images acquired along the <$11\bar{2}0$> zone axis of representative regions of the hex-Ge crystal containing the *I*3 defect either running parallel to the viewing direction (a) or at 60° from the viewing direction (c) The *I*3 defected region is shaded in cyan, the perfect region in red, the overlap region of perfect and defected in green. (**b**) Corresponding intensity profile constructed crossing the atomic planes in the axial direction in the framed regions in (a), where a perfectly stacked hexagonal crystal is framed by a red rectangle and the *I*3 defected region is framed in cyan. (**d)** Corresponding intensity profile constructed the same way as in (b) for the framed regions in (c). The three intensity profiles show no noticeable difference in the spacing of the atomic planes nor dips in the intensity at the positions of the crystal planes that could hint at the absence of material.

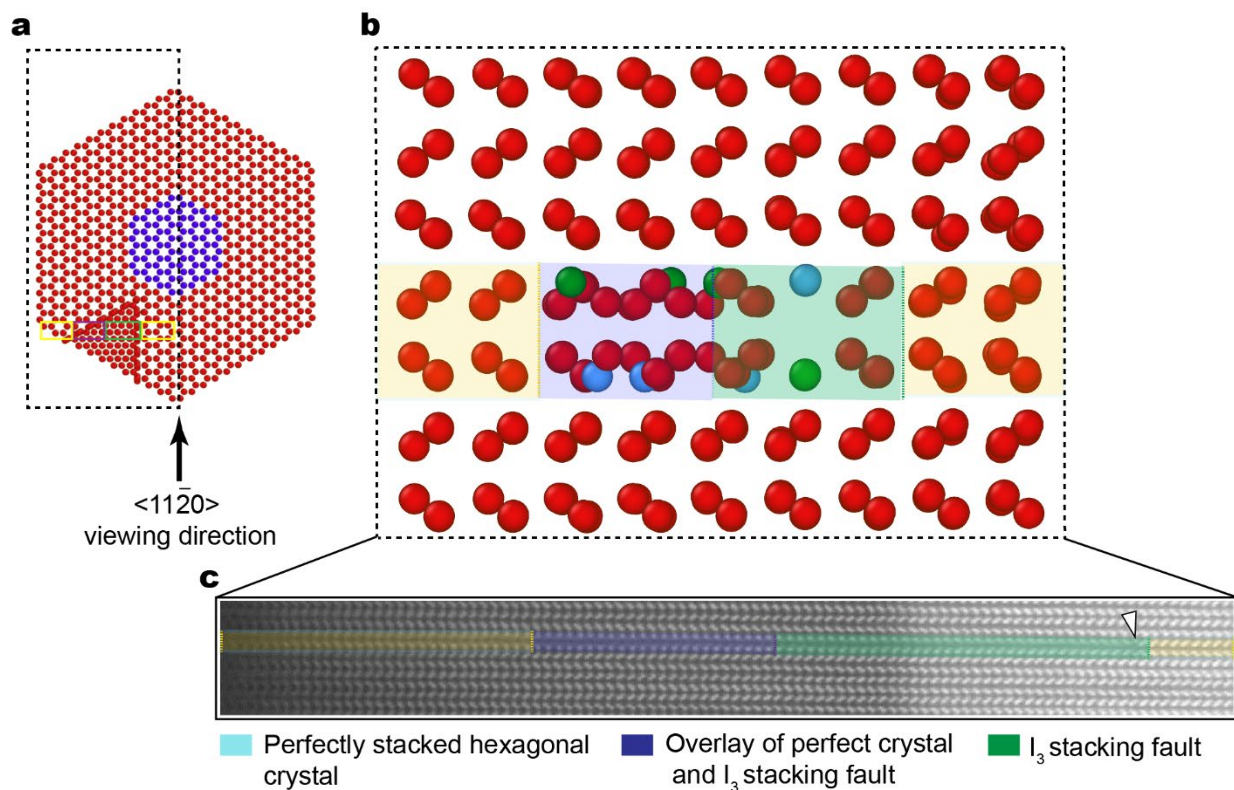

Supporting Figure 6: **Summary of the Different Projected Atomic Configurations of the I_3 BSF and its Terminating Dislocations:** (**a**) A top-view atomic model explaining the planar extension of the I_3 BSF and its terminating dislocations when analyzing the structure in the <$11\bar{2}0$> direction. (**b**) A side-view atomic model corresponding to the black-framed region in (a). (***c****) A* HAADF-STEM image for the highlighted regions in (a, b). The *unhighlighted regions* display perfectly stacked planes showing the ABAB stacking. The green region shows the I_3 stacking fault starting where the white arrow points. The blue region shows the superposition of a perfectly stacked volume with an I_3 defect stacked region in the depth of view. Because of the dislocation line inclined orientation of one of the two I_3 dislocations, the ratio of the perfect/defected volume changes laterally, yielding a gradual change in projected atomic arrangement.

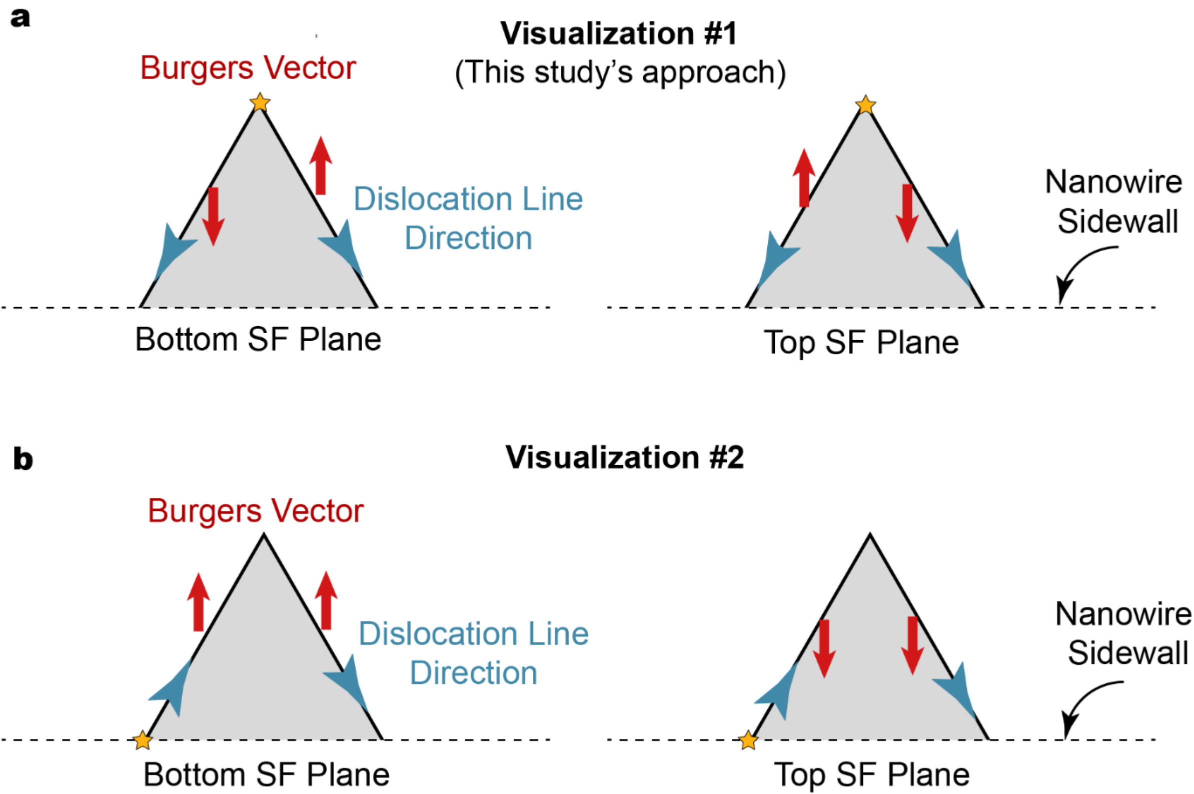

Supporting Figure 7: **Visualization of the Double Plane Stacking Fault: (a) Visulaization #1** (the visualization used in our manuscript): A sketch of the stacking fault in each plane such that the origin of the dislocations in each defected plane is considered the apex of the 60° angle, encompassing the stacking fault (nucleation point of the defect), as indicated by the star. In this case, the dislocations are four independent segments, and the corresponding Burgers vectors are indicated in the sketch by red arrows. **(b) Visualization #2**: A sketch of the stacking fault in each plane such that it is terminated by a semi-loop of a single partial dislocation with constant Burgers vector and uniform clockwise dislocation line direction. The semi loops of each plane are of opposite Burgers vector.

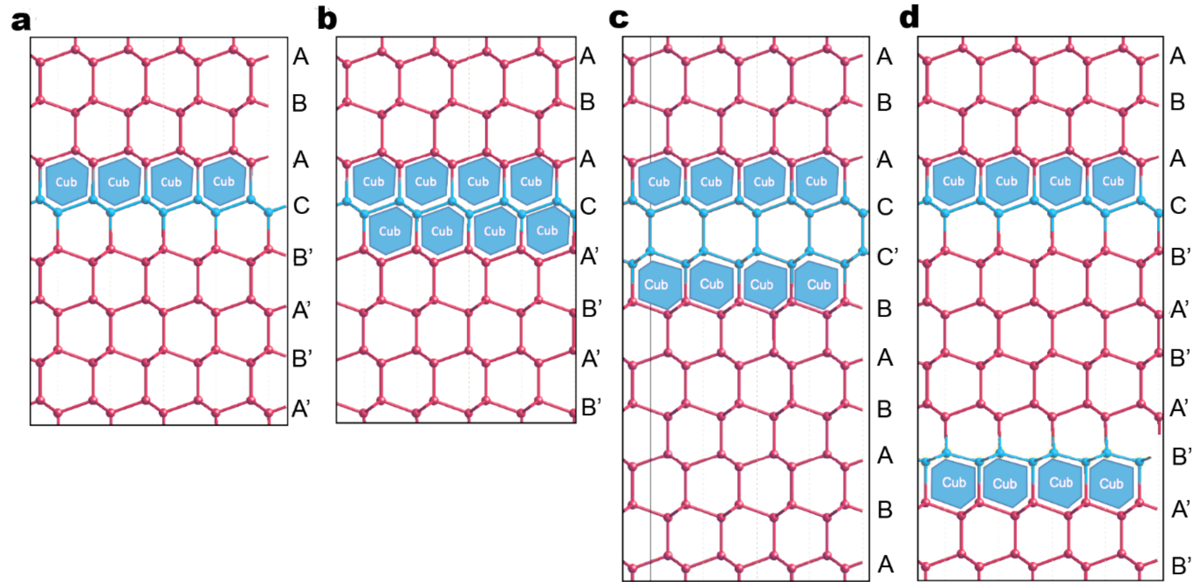

Supporting Figure 8: Different Types of BSFs in a Slab of Hex-Ge: (a, b) with a single stacking fault in two different configurations and forming one or two rows of cubic sites, respectively. (**c**) With the I_3 BSF. (**d)** With two separate single SFs and still forming two rows of cubic sites. The SF plane is highlighted by light blue colored bonds. The *cubic* sites are marked in the figures, and with 'Cub' we indicate the cubic local symmetry, in agreement with the h-c *Jagodzinski* notation. The *hexagonal* symmetry of all the other pristine stacking layers is not explicitly indicated in the figure.

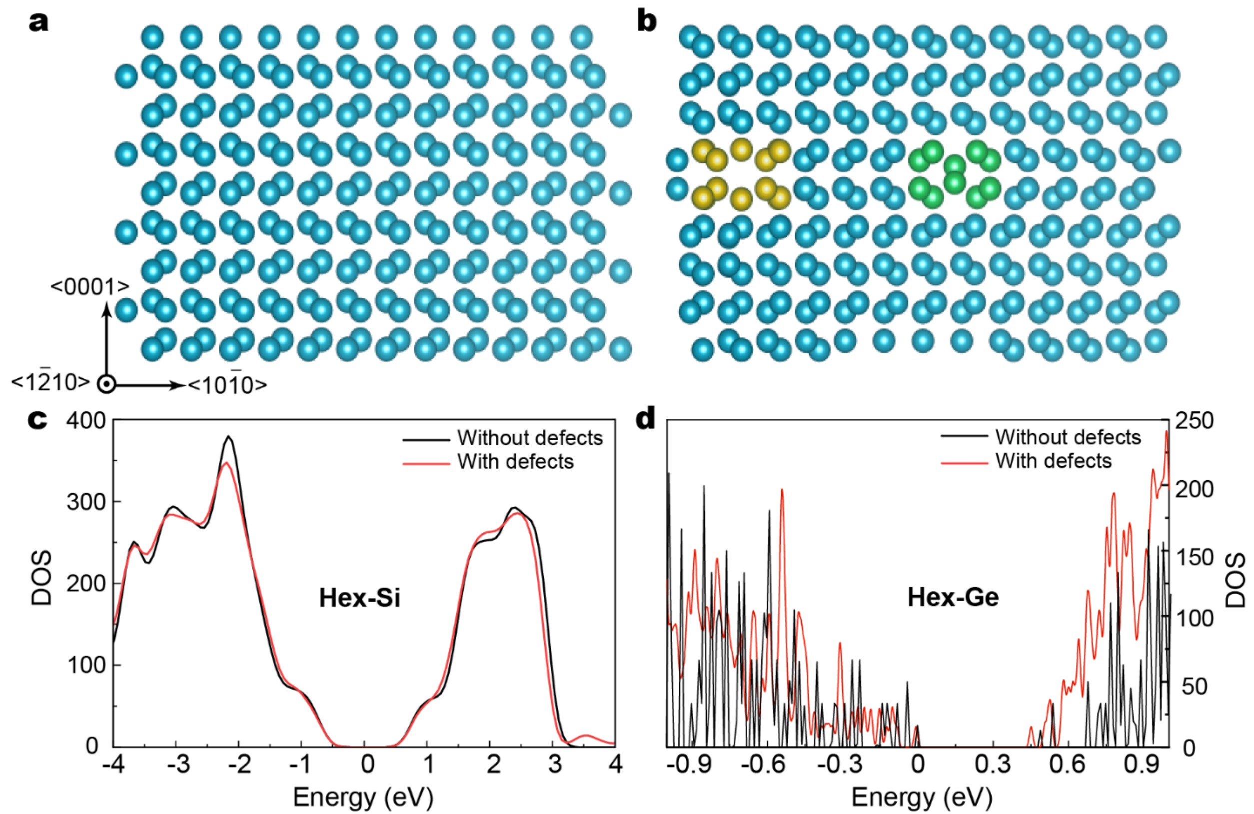

Supporting Figure 9: Band Structure Calculation of Hex-Si and Hex-Ge Crystals With and Without I_3 BSFs and its Terminating Dislocations: based on atomic models of (**a)** A defect-free hex-Si supercell composed of 384 atoms where Si atoms are colored in light blue. (**b)** A hex-Si supercell composed of 384 atoms as well with an I_3 BSF and the terminating dislocations embedded in the supercell. The partial dislocation actually terminating the I_3 BSF is colored in yellow. The green-colored atoms represent a butterfly-like defect that has been introduced in the supercell to preserve the periodicity for the band structure calculations, being impossible to implement the real triangular shape of the defect. Indeed, it is worth mentioning that in our material systems, hex-Ge and hex–Si, only the I_3 BSF with the dislocation pair colored in yellow has been observed, and the butterfly-like defect has never been observed. (**c, d)** Plots showing the calculated density of states (DOS) as a function of the energy of the simulated supercells in (a) and (b) for both Si and Ge with and without defects, respectively. The two curves are similar, and there is not shift at Fermi energy, confirming that the I_3 defect has no mid-gap states associated with it in both materials systems.

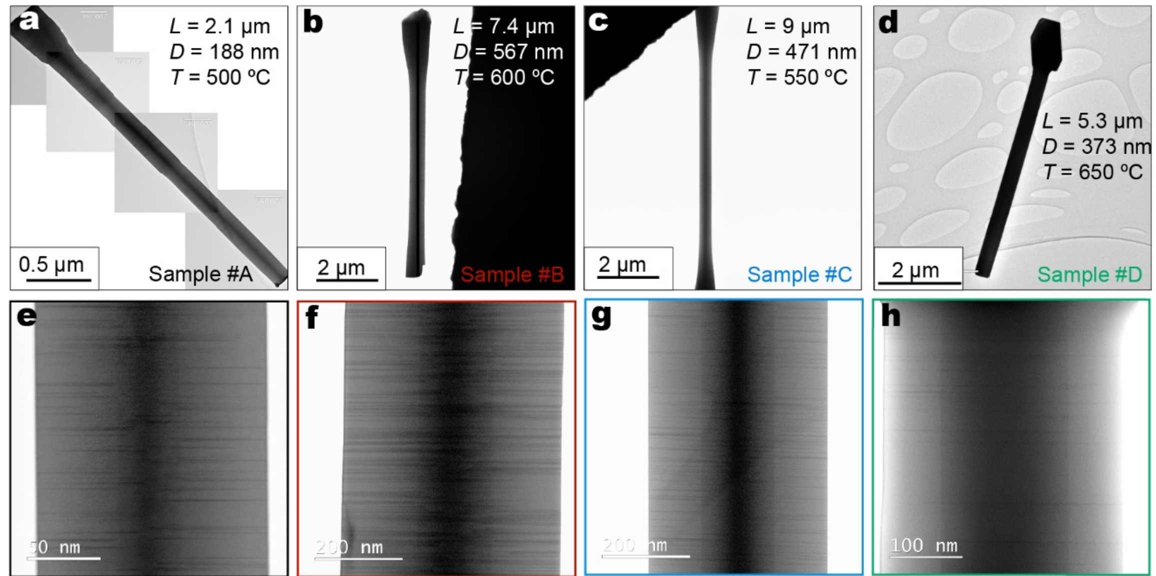

Supporting Figure 10: Representative TEM images of the Characterized Samples by Raman Spectroscopy: Low and high magnification BF-TEM images of the WZ-GaAs/Hex-Ge core/shell structures presented **in Figure. 4** in the main text**.** These samples are of different volumes and fabricated under different conditions resulting in different I_3 stacking faults density. **(a, e)** Sample #A with an I_3 BSFs volume fraction of 4 ± 1.4% **(b, f)** Sample #B with an I_3 BSFs volume fraction of 2.4 ± 0.6%, **(c, g)** Sample #C with an I_3 BSFs volume fraction of 1.6 ± 0.2%, and **(d, h)** Sample #D with an I_3 BSFs volume fraction of 0.2% and assumed to be nearly I_3 defect free. The dimensions of the structures (total structure diameter (D_l) and segment length (L) and growth temperature (T)) are indicated on the images in (a-d).

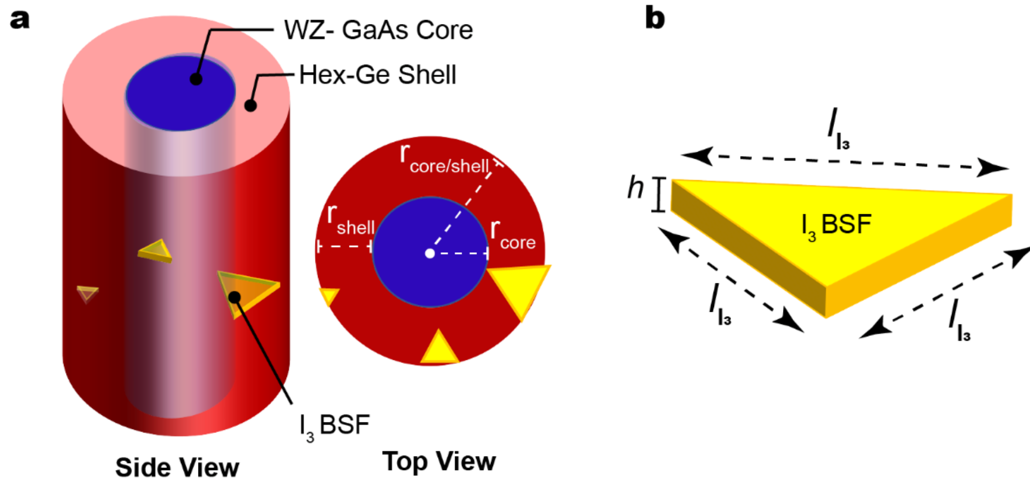

Supporting Figure 11: Defects Quantification and Volume Fraction Calculation: **(a)** Schematic illustration of the core/shell (blue/red) nanowire structure approximated as two concentric circular cylinders. (**b)** The I_3 BSFs, illustrated in yellow, are represented as triangular prisms with an equilateral triangular base of a side length equivalent to the radial extension length for the I_3 BSF in the shell (l_{I3}) and a height (h) of 4-atomic layers of the previously discussed stacking ABCBA.

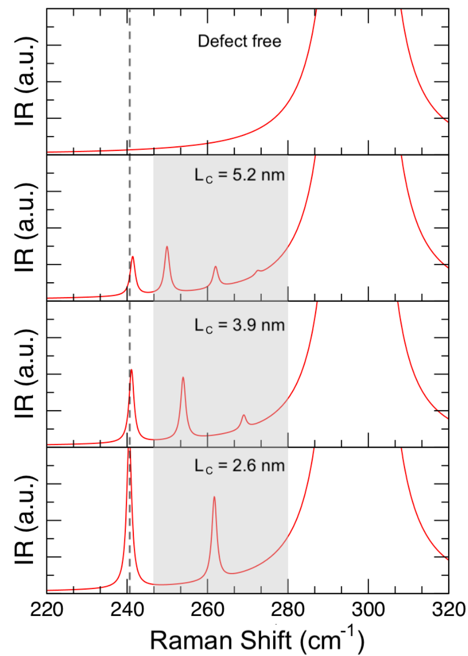

Supporting Figure 12: Theoretically Calculated Raman Spectra of Defect free and I_3 Defected hex-Ge cells: DFPT computed Raman spectra in the zz scattering geometry of, from top to bottom, non-defected hex-Ge, hex-Ge with a stacking fault in a 1×1×4, in a 1×1×6, and in a 1×1×8 supercell. L_c is the distance between the stacking faults imposed by periodic boundary conditions (namely, between the stacking faults). The dashed line emphasizes that the position of the peak at ~240 cm^{-1} is essentially independent on the computational cell size.